
The Phenomenology of Hallucinations

Valeria Ruscio¹ Keiran Thompson¹

Abstract

We show that language models hallucinate not because they fail to detect uncertainty, but because of a failure to integrate it into output generation. Across architectures, uncertain inputs are reliably identified, occupying high-dimensional regions with $2\text{-}3\times$ the intrinsic dimensionality of factual inputs. However, this internal signal is weakly coupled to the output layer: uncertainty migrates into low-sensitivity subspaces, becoming geometrically amplified yet functionally silent. Topological analysis shows that uncertainty representations fragment rather than converging to a unified abstention state, while gradient and Fisher probes reveal collapsing sensitivity along the uncertainty direction. Because cross-entropy training provides no attractor for abstention and uniformly rewards confident prediction, associative mechanisms amplify these fractured activations until residual coupling forces a committed output despite internal detection. Causal interventions confirm this account by restoring refusal when uncertainty is directly connected to logits.

1. Introduction

Language models hallucinate: they generate fluent, confident responses to questions they cannot answer, producing fabricated facts with the same certainty as genuine knowledge. Diffusion models exhibit analogous failures, rendering impossible geometries or contradictory scenes with photographic realism. Despite substantial progress in model scale and alignment, hallucination remains a persistent failure mode. Larger models exhibit reduced frequency of hallucination but do not eliminate it, and instruction tuning encourages hedging without reliably preventing confident errors.

The common view frames hallucination as a knowledge or retrieval problem. We propose a different account. Through

¹Intuition Machines. Correspondence to: Valeria Ruscio <valeria.ruscio@intuitionmachines.com>, Keiran Thompson <keiran@intuitionmachines.com>.

geometric analysis spanning autoregressive transformers, diffusion models, and training dynamics from initialization to alignment, we show that hallucination arises not from missing knowledge but from *geometric compartmentalization*: a systematic disconnect between internal detection of uncertainty and its influence on output behavior. Models reliably recognize when inputs are unanswerable, yet this information fails to propagate to generation.

During training, the gradient of the next-token cross-entropy loss reinforces confident prediction regardless of epistemic status. For factual inputs, this signal increases probability mass on the correct continuation. For impossible or under-specified inputs, it instead reinforces whatever continuation the data distribution associates with the prompt. In neither case does the objective provide an explicit mechanism for expressing uncertainty. As a result, optimization consistently rewards decisive outputs, even when no grounded answer exists.

Our analysis shows the geometric consequences: models develop robust internal representations that separate answerable from unanswerable queries early in processing. However, uncertainty is encoded in high-dimensional subspaces that are weakly coupled to the output layer, allowing it to be processed internally without affecting token probabilities. These representations fragment topologically, while associative mechanisms amplify partial activations. When activation magnitude grows sufficiently, residual coupling to output-sensitive directions produces confident generations.

2. Related Works

The tendency of language models to generate fluent but unfaithful content has been extensively documented across summarization (Maynez et al., 2020), question answering (Lin et al., 2021; Zhang et al., 2023), and open-ended generation (Ji et al., 2022). Some explanations involve exposure bias, knowledge gaps (Kandpal et al., 2022), and expressiveness bottlenecks, with mitigation strategies focusing on retrieval augmentation (Lewis et al., 2020), improved decoding (Lee et al., 2022), and curated fine-tuning (Liu et al., 2024). Recent work has shifted toward analyzing internal model states. Farquhar et al. (2024) introduced semantic entropy for detecting confabulations in meaning space, while multiple studies have shown that hidden representations encode truthfulness signals exploitable for detection (Azaria

& Mitchell, 2023; Chen et al., 2024; Su et al., 2024; Sriraman et al., 2024). At the neuron level, Gao et al. (2025) identified a remarkably sparse subset of neurons (less than 0.1% of total) that reliably predict hallucinations and are causally linked to over-compliance behaviors, with these neurons already present in pretrained base models. Suresh et al. (2025) traced hallucination origins through sparse autoencoders. Complementary work on weight-space structure shows that memorization and fact retrieval occupy specialized directions distinguishable via loss curvature (Merullo et al., 2025), while persona-related behaviors cluster along an interpretable ‘‘Assistant Axis’’ whose deviations predict harmful drift (Lu et al., 2026). Orgad et al. (2024) revealed that models may encode correct answers internally yet consistently generate incorrect ones, a finding with implications for mitigation design. Cohen et al. (2024) proposed explicit uncertainty expression through a learned [IDK] token that shifts probability mass away from uncertain predictions, while Ren & Sutherland (2024) analyzed fine-tuning dynamics to explain how hallucinations strengthen when models inappropriately transfer response patterns across contexts.

3. Methodology

Datasets For language models, we use three evaluation sets: (i) *Factual* 500 manually verified factual questions (generated with Gemini and Claude) on which models exceed 85% accuracy; (ii) *Impossible* 2000 manually verified impossible questions, including underspecified and false-presupposition prompts, probing uncertainty detection; and (iii) a *Hallucination* set combining TruthfulQA with long-tail PopQA, where model accuracy is 20–30%. For diffusion models, we curate 500 paradoxical prompts targeting known failure modes (e.g., clocks, text, counting, spatial coherence), paired with a matched control set of standard scene descriptions. A sample of the datasets is in the appendix A.6.

Geometric Analysis Our analytical framework rests on a core construct: the boundary vector, which operationalizes the abstract notion of ‘‘uncertain information’’ as a concrete geometric direction that we can probe, perturb, and track through the network. At each layer l , we compute the centroid of hidden states for factual inputs μ_l^F and for uncertain inputs μ_l^U , restricting attention to the final token position where next-token prediction occurs in autoregressive models or using spatial means for diffusion latents. The boundary vector is then defined as:

$$b_l = \frac{\mu_l^U - \mu_l^F}{\|\mu_l^U - \mu_l^F\|} \quad (1)$$

This unit vector points from the region of representation space occupied by answerable queries toward the region occupied by unanswerable queries. Movement along b_l corresponds to movement along the axis of answerability

as encoded in the model’s internal representations. We track two properties of this boundary across layers: the boundary norm $\|\mu_l^U - \mu_l^F\|$, measuring raw Euclidean separation between class centroids, and the boundary stability $\cos(b_l, b_{l-1})$, measuring directional consistency across adjacent layers. Growth in boundary norm indicates that the model amplifies the distinction between input types as processing proceeds; high stability indicates that the same geometric direction encodes answerability throughout the network, while low stability signals rotation that may indicate transitions in how uncertainty is represented.

Beyond location, we characterize the local geometry of representations within each input class to test whether the model’s internal organization reflects epistemic status, whether representations of uncertain queries differ systematically in shape, not just position. Local Intrinsic Dimensionality (LID)¹ estimates the effective number of degrees of freedom in the neighborhood of each representation. For a point x with k nearest neighbors at distances $r_1 \leq r_2 \leq \dots \leq r_k$, the maximum likelihood estimate is $\text{LID}(x) = -\left(\frac{1}{k} \sum_{i=1}^k \log \frac{r_i}{r_k}\right)^{-1}$. We compute this for each hidden state and average within input classes, using $k = \min(20, N - 2)$ where N is sample size, adding small Gaussian noise to prevent numerical instability from near-duplicate points. High LID indicates that representations occupy a high-dimensional manifold locally, while low LID indicates concentration on a lower-dimensional structure.

We perform spectral analysis on the covariance of hidden-state representations to characterize the geometry of the sample manifold within each input class. For a given class \mathcal{C} and layer l , we construct the data matrix consisting of the final-token hidden states for all N samples in the class. We compute the eigenvalues of the covariance matrix. Isotropy, defined as the ratio λ_2/λ_1 of the second to first principal component variances, measures how uniformly variance distributes across directions. We compute the effective dimensionality as the exponential of the spectral entropy $N_{eff} = \exp(-\sum_i \hat{\sigma}_i \log \hat{\sigma}_i)$, where $\hat{\sigma}_i$ is the normalized i -th singular value, provides a continuous measure of effective dimensionality: higher entropy indicates information spreads across more dimensions rather than concentrating in a few. We also report the number of principal components required to explain 90% of the total variance as a threshold-based metric of manifold complexity.

For sufficiently separated input classes, we apply persistent homology to characterize the topological structure of representations near the geometric boundary. We select points within a quantile threshold of the boundary, construct the Vietoris-Rips complex (Hausmann, 1996) across a range of distance scales, and record Betti numbers: β_0 counts

¹While absolute LID values depend on k , the relative ratio between uncertain and factual inputs remains robust across a range of $k \in [10, 50]$ and across different model architectures.

connected components while β_1 counts loops. If uncertain representations formed a coherent “I don’t know” cluster, we would expect $\beta_0 = 1$ throughout processing. In practice, we often see $\beta_0 > 100$.

Functional Probes We compute the *Local KL Sensitivity* to measure the robustness of the output distribution to perturbations along the boundary, this metric acts as a finite-difference proxy for the directional Fisher information². For the boundary vector b_l at layer l , we estimate $F(b_l) \approx \frac{1}{2} D_{\text{KL}}^{\text{sym}} [p(y|h_l) \| p(y|h_l + \epsilon b_l)]$ where $D_{\text{KL}}^{\text{sym}}$ is symmetrized KL divergence, ϵ is a small perturbation magnitude, and estimates are averaged over samples within each input class. We implement this by registering forward hooks that add ϵb_l to the hidden state, then comparing output distributions with and without perturbation. Perturbations are applied to post-residual hidden states at the final token position and we choose a fixed $\epsilon = 10^{-3}$ to stay within the numerical precision limits of FP16 while approximating the local linear regime.

The Hessian captures the curvature of the loss landscape along the boundary direction, estimated via finite differences as $H(b_l) \approx \epsilon^{-2} [\mathcal{L}(h_l + \epsilon b_l) - 2\mathcal{L}(h_l) + \mathcal{L}(h_l - \epsilon b_l)]$ where \mathcal{L} is negative log-probability of the predicted token. Curvature is estimated via finite differences in the negative log-probability of the fixed unperturbed argmax token $y_0 = \text{argmax}_p(y|h)$, ensuring differentiability even if the top prediction flips. Positive curvature indicates a cost to moving along the boundary; zero curvature indicates flatness. If the loss landscape is flat along the boundary, the model receives no learning signal to connect its geometric detection of uncertainty to output behavior.

We also measure how perturbations along the boundary propagate through each layer. The Jacobian amplification of the full transformer block, defined as $\text{amp}_l = \epsilon^{-1} \|\text{Layer}_l(h + \epsilon b_l) - \text{Layer}_l(h)\|$, estimates changes in the layer’s Jacobian along the boundary direction. Values greater than one indicate the layer magnifies boundary perturbations; values less than one indicate attenuation. Late-layer amplification is particularly significant: if final layers act as confidence amplifiers that magnify whatever signal is present regardless of epistemic status, then even weak associative guesses will be scaled into confident predictions. To test whether the model has learned a pathway from internal detection to appropriate output, we examine gradient flow from uncertainty-related tokens. We define a set of target tokens associated with uncertainty expression (“unsure,” “unknown,” “maybe,” “approximately,” and more) and compute the gradient of their summed logits with respect to hidden states at each layer. The gradient blockage metric is the cosine similarity between this gradient and

²Since this metric captures the local curvature properties typically associated with the Fisher information matrix, we refer to it as *Fisher sensitivity* (F) in the analysis.

the boundary vector: $\text{blockage}_l = \cos(\nabla_{h_l} \sum_{k \in \mathcal{U}} z_k, b_l)$. Positive values indicate that increasing uncertainty-token probability would push representations toward the uncertain region, as expected. Near-zero values indicate geometric decoupling: uncertainty expression and boundary position are orthogonal, explaining why internal detection fails to reach output despite being present in representation space. Finally, we examine how the boundary couples to the output map. The unembedding matrix $W_U \in \mathbb{R}^{V \times d}$ maps hidden states to vocabulary logits. Rather than appealing to an exact null space (which can be trivial when W_U is full rank), we characterize output sensitivity via its singular structure: $W_U = U\Sigma V^T$, with singular values $\sigma_1 \geq \dots \geq \sigma_d$. For a cutoff m , we define the visible subspace $\mathcal{V}_m = \text{span}\{v_1, \dots, v_m\}$ and its complement \mathcal{V}_m^\perp . We measure boundary visibility as $\text{vis}_m(b_l) = \frac{\|P_{\mathcal{V}_m} b_l\|}{\|b_l\|}$, and its complement as $\text{lowSens}_m(b_l) = \frac{\|P_{\mathcal{V}_m^\perp} b_l\|}{\|b_l\|}$. We report robustness curves over m . Low visibility for moderate m indicates that the boundary predominantly occupies directions with low gain under W_U , i.e., directions that minimally affect logits despite potentially large hidden-state magnitude. This provides a geometric explanation for compartmentalization: uncertainty is encoded in subspaces that are weakly coupled to vocabulary output, allowing it to be processed internally without influencing token probabilities. We apply the same decomposition to the hidden states, computing $\text{LowSens}_{\text{ratio}}(h_l) = \|P_{\mathcal{V}_m^\perp} h_l\| / \|P_{\mathcal{V}_m} h_l\|$, to quantify how much representational energy resides in low-output-sensitivity directions across layers and training checkpoints.

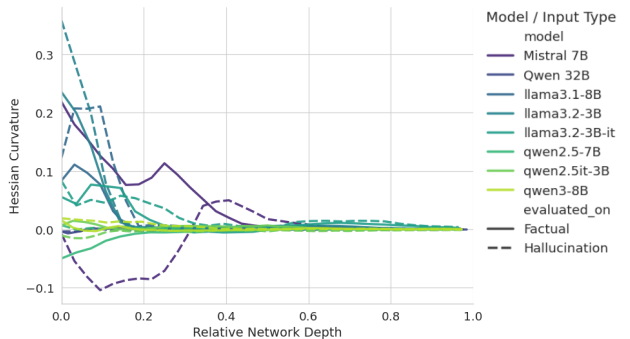


Figure 1. Hessian curvature of Factual vs Hallucination inputs across multiple architectures.

Activation Dynamics and Component Analysis We trace the dynamic flow of representations through network components to identify where uncertainty-related structure emerges and where its influence on output weakens. For each attention head, we compute the entropy of the attention distribution $H_{\text{head}} = -\sum_j \alpha_j \log \alpha_j$ where α_j is the attention weight from the final token to position j . High entropy indicates diffuse attention, reflecting ambiguity in retrieval or evidence localization, while low entropy indi-

cates focused attention on specific positions. We compare these distributions across input classes and separately track attention to the first token (the attention sink as in (Ruscio et al., 2025)), testing whether differential sink behavior correlates with input type.

To study which components most strongly contribute to class separation, we decompose residual-stream updates (omitting layer normalization for clarity) as $h_{l+1} = h_l + \text{Attn}_l(h_l) + \text{MLP}_l(h_l)$. At each layer, we measure alignment between each component’s output and the boundary vector: $\text{atn_align}_l = \cos(\text{Attn}_l(h_l), b_l)$ and $\text{mlp_align}_l = \cos(\text{MLP}_l(h_l), b_l)$. Positive alignment for uncertain inputs indicates that the corresponding component shifts representations toward the boundary direction. Comparing magnitudes across layers reveals whether separation is more strongly reflected in attention outputs (consistent with retrieval-mediated effects) or MLP outputs (consistent with associative transformations). For diffusion models, we additionally track the ratio of cross-attention magnitude (text-to-image) to total attention as a proxy for conditioning strength; collapse of this ratio indicates decoupling from the textual prompt. We track the mean projection of hidden states onto the boundary vector: $\text{proj}_l = \mathbb{E}_{x \in \mathcal{C}}[h_l(x) \cdot b_l]$, computed over samples within each input class \mathcal{C} . The trajectory of this projection reveals whether classes diverge along the boundary as processing proceeds. We also apply the unembedding matrix to intermediate final-token hidden states, obtaining layer-wise “predictions” whose entropy and confidence trajectories indicate when the model commits to specific outputs and whether uncertain inputs exhibit earlier or stronger commitment. For autoregressive models, we analyze token-level signatures at the final position. Kurtosis of final-layer activations measures whether representations are distributed across many features or dominated by outliers; we test whether hallucinations exhibit elevated kurtosis, consistent with reliance on sparse or atypical directions. We compute surprisal of the anchor token and prediction entropy, examining correlations with correctness. Drift is quantified as the cosine similarity between the initial token embedding and its final representation, with lower values indicating greater contextual transformation. For the diffusion model, several adaptations are required. Spatial activations are mean-pooled for geometric metrics, Gini sparsity replaces kurtosis as a more robust measure of feature concentration in high-dimensional latents. Cross-attention analysis tracks conditioning strength across layers.

Causal Interventions To test whether the geometric mechanisms identified in our analysis play a causal role in hallucination, we design three targeted interventions. Table 4 shows tests for (i) leakage of uncertainty representations into active computation, (ii) failure of integration between detection and output, and (iii) high-dimensional fragmentation of uncertain representations. All interventions are

applied to Llama 3.2 3B (Base) at layer 16 and Qwen 2.5 3B (base) at layer 20, the depth at which our geometric analysis indicates the onset of representational fracture. Experiments are run on the Hallucination dataset.

We first test whether the uncertainty boundary direction acts as a causal control axis for model behavior. We define a steering vector $v_{\text{steer}} = \mu^{\mathcal{U}} - \mu^{\mathcal{F}}$ where $\mu^{\mathcal{U}}$ and $\mu^{\mathcal{F}}$ are the centroids of uncertain and factual hidden states at Layer 16. During inference on factual inputs, we inject this vector into the hidden state: $h'_l = h_l + \alpha v_{\text{steer}}$ with scaling factor α . This intervention simulates boundary leakage by forcing activations to move along the uncertainty direction, allowing us to assess whether large excursions along this axis induce degradation or hallucination-like behavior. To test whether uncertainty is internally detected but fails to influence output, we train a linear classifier (logistic regression) on layer-16 (and layer 20) hidden states to distinguish factual from uncertain inputs. At inference time on uncertain samples, we use the classifier’s predicted probability $P(\text{uncertain} | h_l)$ to intervene directly at the output logits: $\text{Logits}_{\text{final}} = \text{Logits}_{\text{model}} + \gamma P(\text{uncertain} | h_l) e_{\text{unsure}}$ where γ is a gain parameter and e_{unsure} is the one-hot vector corresponding to a refusal or uncertainty token (e.g., “unsure”). Finally, we test whether the high intrinsic dimensionality of uncertain representations reflects simple noise or more complex fragmentation. We perform PCA on factual hidden states to define a low-dimensional factual subspace $S_{\mathcal{F}}$ capturing 95% of variance. For uncertain inputs, we project hidden states onto this subspace: $h'_{\text{proj}} = \text{Proj}_{S_{\mathcal{F}}}(h_l - \mu^{\mathcal{F}}) + \mu^{\mathcal{F}}$ and apply a soft interpolation with the original state: $h'_{\text{final}} = (1 - \lambda)h_l + \lambda h'_{\text{proj}}$. This intervention tests whether hallucination-related geometry can be repaired by linear projection onto the structured manifold of factual representations.

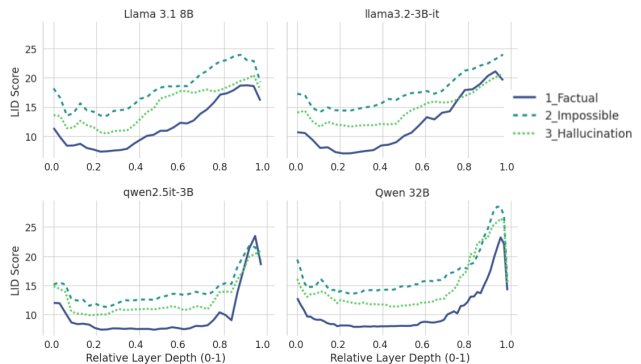


Figure 2. LID as a function of depth for different kinds of input across multiple architectures.

4. Analysis

Our experiments span autoregressive language models (Llama-3.2, Qwen 2.5, Qwen3, Mistral v0.1), diffusion-

based image generation (PixArt- Σ), and developmental trajectories from near-initialization through post-training alignment (Pythia, OLMo checkpoints). Our results on component-level mechanisms A.1 and developmental trajectory A.2 are in the appendix due to space constraint.

Table 1. Despite variations in Attention Entropy and Sink attention, Hallucinations maintain high Residual Stream Norms and Output Confidence levels comparable to Factual inputs.

Model	Cond.	Ent.	Sink	Norm	Conf.
Llama 3.1 (8B)	Fact.	0.96	0.72	18.5	0.047
	Hall.	1.06	0.70	18.8	0.024
	Imp.	1.01	0.70	19.0	0.022
Qwen 2.5 (7B)	Fact.	1.17	0.53	108.0	0.251
	Hall.	1.27	0.52	106.9	0.244
	Imp.	1.17	0.54	109.1	0.268
Qwen 3 (32B)	Fact.	0.66	0.01	329.2	0.269
	Hall.	0.72	0.01	324.4	0.266
	Imp.	0.69	0.01	341.3	0.270

Across all architectures examined, models reliably identify inputs that should trigger uncertainty, geometrically separating answerable from unanswerable queries with high fidelity, but the translation of this internal signal into appropriate output behavior fails. Inputs the model can confidently answer occupy low-dimensional, well-organized regions of representation space, reflecting training-induced compression into efficient feature subspaces. In contrast, inputs that should get uncertainty lie in high-dimensional, diffuse regions that resist compression. This pattern appears consistently across architectures: as shown in Fig. 2, the Local Intrinsic Dimensionality (LID) of uncertain inputs exceeds that of grounded inputs by a factor of 2–3 \times in both autoregressive transformers and diffusion models. Early in training, models partition their representation space into two functional regions: a low-dimensional, vocabulary-aligned *surface* used for immediate token prediction, and a higher-dimensional, weakly vocabulary-coupled *reservoir* used for contextual storage, intermediate computation, and uncertainty encoding. This separation is adaptive, it enables complex internal processing without premature commitment to output, but it also introduces a structural vulnerability. Hallucination emerges through three interacting mechanisms: **Detection** The model correctly identifies uncertain inputs and routes them into the reservoir. Representations separate along a stable boundary direction, with uncertain inputs exhibiting elevated intrinsic dimensionality, high spectral entropy, and low alignment with output-sensitive directions. The geometric signal is unambiguous: these inputs should not produce confident predictions. **Fracture** The uncertainty manifold lacks coherent organization. Rather than converging toward a unified representation of abstention, it fragments topologically into disconnected components. Each fragment drifts toward different regions of

output space. The model does not form a single representation of “I don’t know,” but instead maintains a dispersed collection of partial and competing activations. **Breach** The pathway from detection to expression is functionally severed. Gradients from uncertainty-related tokens fail to align with the boundary direction, and Fisher sensitivity (F) along this axis collapses. Meanwhile, MLP layers, acting as associative pattern-completion mechanisms, amplify activity within the fractured representations. Once activation magnitude becomes sufficiently large, even weak coupling to vocabulary-aligned directions yields substantial logits. Uncertainty, though stored in low-sensitivity subspaces, leaks into output space and crystallizes as confident generation. The manifestation of this breach depends on output modality. Autoregressive language models, constrained to discrete token selection, tend toward feature collapse: the model produces fluent but incorrect responses. Diffusion models, operating in continuous output spaces, preserve the fracture itself: uncertainty renders directly as visual incoherence, artifacts, inconsistent geometry, in other words, hallucinations.

Table 2. Uncertain inputs (Impossible/Hallucination) consistently show higher dimensionality and entropy than Factual inputs.

Model	Bucket	LID	Isotropy	Entropy
Llama-3.1-8B	Factual	11.79	0.66	319.9
	Hallucination	15.09	0.70	618.8
	Impossible	18.05	0.52	664.0
Qwen-2.5-7B	Factual	9.71	0.58	265.7
	Hallucination	12.62	0.51	507.1
	Impossible	14.27	0.41	554.4
Qwen-3-32B	Factual	10.41	0.54	279.2
	Hallucination	14.70	0.54	579.5
	Impossible	16.76	0.52	636.5

The Geometry of Knowledge Across all models examined, uncertain inputs consistently exhibit higher LID than grounded inputs. In LLaMA-3.2 at layer 15, factual inputs show LID ≈ 10.9 versus ≈ 15.8 for hallucinatory inputs (as we can see in Table 2 and 6); in PixArt- Σ at layer 14, coherent prompts yield LID ≈ 5.0 compared to ≈ 12.5 for paradoxical prompts. This 2–3 \times ratio appears consistently across architectures, modalities, and model scales. Factual concepts are compressed by training into efficient representations. Uncertain or paradoxical inputs lack this structure, activating conflicting or absent features and spreading across available dimensions. Elevated dimensionality thus provides a geometric signature of epistemic uncertainty. Complementary metrics reinforce this picture: factual inputs exhibit lower spectral entropy and lower isotropy (λ_2/λ_1), concentrating variance along predictive directions, while uncertain inputs distribute variance more uniformly. Hallucinatory inputs are also geometrically distinct from impossible (confabulatory) queries. In OLMo checkpoints at 100k steps, im-

possible inputs approach isotropy (≈ 0.86), forming nearly spherical, unstructured distributions. Hallucinations retain partial organization (≈ 0.45), indicating ellipsoidal structure with residual directional alignment. The model treats impossible queries as noise, but imposes pseudo-structure on hallucinations by activating partial memories, producing sufficient coherence for generation without supporting accuracy. The boundary norm $|\mu_l^M - \mu_l^F|$ increases monotonically with depth. In Qwen-2.5, separation grows from ≈ 0.33 at layer 0 to ≈ 156 at layer 27, indicating active amplification of epistemic distinctions. The boundary direction itself remains stable: Mistral exhibits cosine similarity exceeding 0.99 between adjacent layers, showing that the same geometric axis encodes answerability throughout the network. Residual projections ($h_l \cdot b_l$) further show that hallucinations occupy an intermediate position between factual and impossible inputs. In Qwen-2.5 at layer 27, we observe $\text{res_proj}_{\text{Fact}} \approx -22.5$, $\text{res_proj}_{\text{Hal}} \approx +93.9$, and $\text{res_proj}_{\text{Imp}} \approx +125.0$. The model correctly positions hallucinations closer to impossibility than fact. Detection succeeds; the failure lies in how this signal influences output.

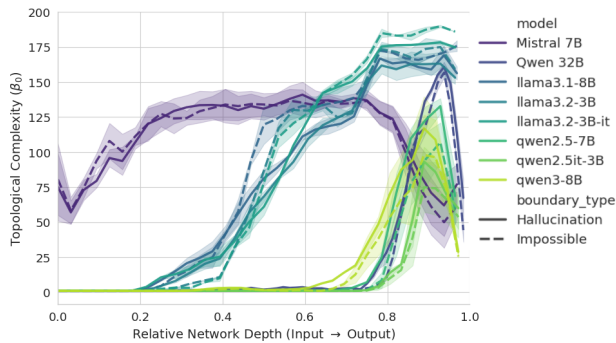


Figure 3. Topological complexity (β_0) evolution by depth across multiple architectures

Topological Fracture Persistent homology shows progressive fragmentation of uncertain representations. In LLaMA-3.2, the zero-th Betti number β_0 increases from 1 at layer 0 to 93 at layer 15 and 119 at layer 27, see Fig. 3, indicating that the uncertainty manifold decomposes into over a hundred disconnected components. If uncertain inputs converged toward a unified refusal state, β_0 would remain near one; instead, the model partitions uncertainty into multiple clusters. This fragmentation provides a geometric mechanism for hallucination: rather than forming a coherent representation of abstention, different fragments drift toward distinct output regions, allowing a single epistemic state to map onto many competing generations. Non-zero first Betti numbers β_1 further indicate topological holes within these components, implying that the boundary separating factual from uncertain inputs is not a simple linear surface but a complex, non-convex structure resistant to linear readout.

The Low Sensitivity Reservoir We quantify alignment between hidden representations and output-sensitive directions using the low-sensitivity subspace of the unembedding matrix. In Pythia near initialization (step 8), representations exhibit uniformly high low-sensitivity ratios (≈ 1.0), indicating minimal coupling to vocabulary. By step 512, a pronounced stratification emerges: early layers (0–4) show ratios near 1.1, while late layers (26–30) reach ≈ 2.87 . The model learns to concentrate high-magnitude activity in directions weakly coupled to output, forming a reservoir that supports internal computation without directly affecting token probabilities. Intermediate checkpoints show the learning dynamics: at step 64, middle layers briefly reduce their low-sensitivity ratio (≈ 0.88), reflecting short-term reliance on direct output-aligned signaling. This phase gives way to a mature regime in which deeper layers perform computation primarily in low-sensitivity directions. At the same time, representation magnitude grows substantially with depth, increasing from ≈ 1.3 at layer 0 to ≈ 20.0 at layer 30. This amplification occurs predominantly along low-sensitivity directions, enabling extensive internal processing while maintaining limited immediate influence on logits. This system introduces a specific vulnerability: under typical conditions, uncertain inputs route into low-sensitivity subspaces, remaining geometrically separated from vocabulary-aligned directions. However, when MLP activations amplify fragmented features, overall magnitude increases. Once sufficiently large, even weak coupling to output-sensitive directions yields substantial logits. In LLaMA-3.2, hallucinations exhibit vocabulary visibility of only ≈ 0.48 , yet boundary norm reaches ≈ 21.5 , allowing the residual aligned component to drive confident prediction. Hallucination thus corresponds to uncertainty leaking from low-sensitivity reservoirs into output space.

Table 3. Random-direction control tests. Steering along the boundary (b) produces larger changes than random directions (r).

Model	Layer	F_b	F_r	KL_b	KL_r	Flip_b	Flip_r
Llama (3.2-3B)	Early	12.76	12.74	2.33	1.20	0.98	0.90
	Mid	10.78	10.63	1.19	0.70	0.79	0.74
	Late	5.85	5.98	0.31	0.18	0.66	0.43
Qwen (2.5-3B)	Early	36.52	37.04	1.70	0.10	0.53	0.27
	Mid	32.91	32.96	0.11	0.08	0.27	0.26
	Late	20.76	19.89	0.05	0.04	0.16	0.15

Loss Landscape Decoupling Despite large geometric separation between factual and uncertain representations, sensitivity of the output distribution along the boundary direction collapses in late layers. In LLaMA-3.2 at layer 27, the boundary norm reaches ≈ 21.5 while Fisher sensitivity (F) drops to ≈ 0.005 , indicating that perturbations along the uncertainty axis produce negligible changes in output probabilities. Training dynamics clarify this effect: in OLMo 7B during pretraining, Fisher sensitivity (F) ini-

tially increases (Step 2k: $F \approx 0.047$, Step 20k: $F \approx 0.060$, Step 50k: $F \approx 0.06$), suggesting that early optimization builds sensitivity to the fact-fiction boundary. The subsequent collapse observed in instruction-tuned models (Llama 3.2 3B it, qwen 2.5 3B it) indicates that alignment stages suppress this sensitivity. Gradient blockage further confirms this decoupling: in trained models, gradients from uncertainty-related tokens show near-zero cosine alignment with the boundary direction, indicating that uncertainty detection does not propagate to output. OLMo checkpoints show partial construction of this pathway during pretraining (Step 2k: $\text{grad_block} \approx 0.02$ and Step 50k: $\text{grad_block} \approx 0.12$), but the effect remains insufficient to counteract competing generative pressures. In Pythia at step 512, Fisher sensitivity (F) decreases by 63% from layer 0 to layer 30. As representations migrate into low-sensitivity subspaces, output becomes increasingly insensitive to deep-layer perturbations. This explains why topological fracture fails to trigger abstention: the fractured uncertainty manifold resides in directions to which the readout is largely unresponsive.

Causal Intervention Across both architectures we tested (Llama 3.2 3B and Qwen 2.5 3B), the readout bypass intervention converts internal uncertainty detection into explicit refusal with near-perfect reliability. As we can see in Table 4, in both cases, a linear probe trained solely on hidden-state geometry is enough to identify uncertain inputs and force appropriate output behavior. The success of a linear probe confirms that the epistemic state is not only present but linearly separable, implying that the model’s failure to refuse is a failure of downstream integration, not representational capacity; hallucination arises from a severed detection-expression pathway, not a failure of detection. Injecting the boundary direction into factual inputs reliably alters model behavior, confirming that this direction constitutes a causal control axis. Steering changes the output in 99.75% of LLaMA cases and 89.36% of Qwen cases, indicating that the extracted uncertainty direction is not incidental but tightly coupled to generation. However, the qualitative response differs sharply between models, this suggests distinct architectural responses to high-energy uncertainty perturbations. In the framework of our geometric analysis, LLaMA tends toward a high-entropy “guessing” regime, whereas Qwen preferentially enters a “confident hallucination” regime. Projecting uncertain representations onto the low-dimensional factual subspace does not reduce pathological behavior in either model. In LLaMA, loop rate increases from 9.85% to 12.88%; in Qwen it remains unchanged at 1.77%. This negative result is informative: if uncertainty were merely additive noise around a factual manifold, linear projection would be expected to restore coherence. The failure of PCA repair, combined with our persistent homology results, suggests that the uncertainty representation is not just a linear displacement of factual

states, but likely involves non-convex or topographically complex structures.

Cross-Architecture Comparison PixArt- Σ exhibits the same geometric signature of uncertainty observed in autoregressive models: at layer 14, coherent prompts show LID ≈ 5.0 compared to ≈ 12.5 for paradoxical prompts, preserving the 2-3 \times ratio across modalities. Both architectures encode uncertainty as local dimensional expansion. The confusion-alignment metric in PixArt parallels drift cosine in language models: coherent concepts show strong orthogonal rejection (≈ -25.9), while paradoxical concepts drift closer (≈ -21.7), indicating successful internal detection in both systems.

Autoregressive models (discrete output) constrained to select a token, language models cannot sustain high-dimensional uncertainty. Representations collapse onto sparse directions, reflected in extreme activation kurtosis as a small number of features dominate. The fragmented manifold projects onto arbitrary vocabulary items, producing fluent but incorrect outputs. **Diffusion models** (continuous output) in contrast, diffusion models preserve high-dimensional uncertainty. In PixArt- Σ , Gini sparsity evolves similarly for coherent and paradoxical prompts (0.44 \rightarrow 0.58), indicating no feature collapse. Instead, the model enters a drift regime: cross-attention to text decreases from ≈ 0.03 to ≈ 0.001 by layer 27, while self-attention continues refinement without grounding. The high-LID geometry therefore manifests directly as visual incoherence. Near-zero cross-attention in late layers implies minimal reference to the prompt. Structural errors introduced at intermediate layers (where LID peaks) are subsequently refined rather than corrected, yielding plausible but inconsistent images.

5. Random-direction controls

To verify that the observed effects are specific to the uncertainty boundary and not generic properties of high-dimensional representations, we perform a random-direction control. At each layer, we compare perturbations along the learned boundary vector b_l with perturbations along a random orthogonal vector r_l scaled to match the norm of b_l . We evaluate three quantities across early, middle, and late layers: (i) Fisher sensitivity (F), measured as KL divergence under small perturbations; (ii) steering strength, measured by KL divergence and top-1 probability flips under large perturbations; and (iii) gradient alignment between uncertainty-token logits and the boundary direction. Results are summarized in Table 3.

In both Llama-3.2-3B and Qwen-2.5-3B, steering along the boundary produces substantially larger output changes than random directions, though the critical depth varies by architecture). Boundary perturbations induce higher KL divergence and higher output flip rates than random

Table 4. Causal Intervention Results

Model	Readout Bypass		Boundary Steering		Manifold Repair	
	Baseline Refusal	Bypass Refusal	Output Change	Loop Rate	Baseline Loop	Repaired Loop
Llama 3.2 3B	0.00%	100.00%	99.75%	55.45%	9.85%	12.88%
Qwen 2.5 3B	0.00%	99.75%	89.36%	16.09%	1.77%	1.77%

controls, confirming that the boundary constitutes a genuine causal axis rather than incidental noise. Despite large boundary norms, Fisher sensitivity (F) remains comparable between boundary and random directions. This indicates that locally, representations lie in low-sensitivity subspaces: small movement along the uncertainty boundary produces no greater output change than movement along an arbitrary direction. Across both architectures, gradient alignment between uncertainty-token logits and the boundary direction remains near zero at all depths. This confirms a systematic integration failure: although uncertainty is geometrically detected, training gradients do not reinforce its expression. The detection signal is present but decoupled from output. Llama exhibits higher late-layer steering flip rates, reflecting brittle feature collapse under uncertainty. Qwen shows lower flip rates but comparable Fisher sensitivity (F) collapse, indicating more stable but confident hallucination.

6. Optimization pressure and uncertainty collapse

Modern generative models are trained to minimize the Kullback-Leibler (KL) divergence between their output distribution and a target distribution defined by the training data. For logits $z \in \mathbb{R}^V$ and a one-hot target y , this simplifies to minimizing the negative log-likelihood $\mathcal{L}(z, y) = -\log(\frac{\exp(z_y)}{\sum_j \exp(z_j)})$. The gradient of this loss with respect to the logit z_i is given by: $\nabla_z \mathcal{L} = \mathbf{p} - \mathbf{y}$ where \mathbf{p} is the softmax probability vector and \mathbf{y} is the one-hot target. So, this gradient vanishes only when $\mathbf{p}_y \rightarrow 1$. Because the softmax function is asymptotic, achieving $\mathbf{p}_y = 1$ requires the logit difference $z_y - z_{j \neq y}$ to approach infinity. So, the training objective exerts a constant, non-vanishing pressure to increase the norm of the logit vector $\|z\|$ and concentrate probability mass on a single token. This creates a “runaway confidence” dynamic: the loss landscape contains no local minima corresponding to high-entropy (uncertain) states. Even in regimes of genuine data ambiguity, the gradient descent process treats uniform distributions not as valid epistemic representations, but as high-loss states requiring further optimization toward a vertex of the probability simplex. Geometrically, this creates a *Simplex Vertex Attractor*. The softmax output lives on a $(V - 1)$ -dimensional simplex where vertices correspond to deterministic predictions and the centroid corresponds to maximum uncertainty (unfor-

mity). Cross-entropy loss against one-hot targets renders the vertices the only global minima. Training effectively partitions the representation space into Voronoi cells (Aurehammer & Klein, 2021) centered on vocabulary embeddings. To minimize loss, the model must push representations deep into the interior of these cells, maximizing the margin to the decision boundary (Gunasekar et al., 2018). Without an explicit “abstention” targets or distributional labels, uncertain inputs are subject to the same geometric forces as factual ones: they are projected away from the simplex center and forced to collapse into the nearest vocabulary basin. This mechanism could explain the “decoupling” observed in our empirical analysis. The model may successfully encode uncertainty in the *direction* of the hidden state (as detected by our boundary metrics), but the *magnitude* amplification driven by the training objective washes out this signal at the readout layer. Unless the uncertainty direction is explicitly orthogonalized against the readout matrix W_U , the pressure to maximize logit separation will use these features to support a guess.

7. Conclusion

We presented a geometric account of hallucination that re-frames the phenomenon as a failure of integration rather than detection. Models identify inputs that warrant uncertainty, yet they fail to express it. Such inputs occupy high-dimensional regions of representation space, separated from factual queries along a stable boundary direction that is amplified across layers. Yet this geometric signal never reaches output. Instead, uncertainty fractures into disconnected components, migrates into subspaces weakly coupled to vocabulary, and becomes invisible to the loss as Fisher sensitivity along the boundary collapses. Guided by this analysis, we outline geometry-aware interventions in Appendix A.4. Hallucination is shown to be a predictable consequence of training objectives that reward confident generation while providing no mechanism for uncertainty expression.

8. Acknowledgments

We thank Eli-Shaoul Khedouri for helpful discussions.

Impact Statement

This paper presents work whose goal is to advance the field of Machine Learning. There are many potential societal consequences of our work, none which we feel need be specifically highlighted here. We hope that an improved understanding of the Hallucination phenomenon will enable the development of more trustworthy LLMs.

References

- Ansuini, A., Laio, A., Macke, J. H., and Zoccolan, D. Intrinsic dimension of data representations in deep neural networks. In *Neural Information Processing Systems*, 2019. URL <https://api.semanticscholar.org/CorpusID:170079070>.
- Aurenhammer, F. and Klein, R. Voronoi diagrams. In *Handbook of Computational Geometry*, 2021. URL <https://api.semanticscholar.org/CorpusID:7101732>.
- Azaria, A. and Mitchell, T. M. The internal state of an llm knows when its lying. *ArXiv*, abs/2304.13734, 2023. URL <https://api.semanticscholar.org/CorpusID:258352729>.
- Chen, C., Liu, K., Chen, Z., Gu, Y., Wu, Y., Tao, M., Fu, Z., and Ye, J. Inside: LLMs’ internal states retain the power of hallucination detection. *ArXiv*, abs/2402.03744, 2024. URL <https://api.semanticscholar.org/CorpusID:267499843>.
- Chen, W. Universal topological marker. *Physical Review B*, 2022. URL <https://api.semanticscholar.org/CorpusID:252438774>.
- Cohen, R., Dobler, K., Biran, E., and de Melo, G. I don’t know: Explicit modeling of uncertainty with an [idk] token. *ArXiv*, abs/2412.06676, 2024. URL <https://api.semanticscholar.org/CorpusID:274597439>.
- Efanov, A. A., Ivliev, S., and Shagraev, A. G. Welford’s algorithm for weighted statistics. *2021 3rd International Youth Conference on Radio Electronics, Electrical and Power Engineering (REEPE)*, pp. 1–5, 2021. URL <https://api.semanticscholar.org/CorpusID:233177366>.
- Elhage, N., Nanda, N., Olsson, C., Henighan, T., Joseph, N., Mann, B., Askell, A., Bai, Y., Chen, A., Conerly, T., DasSarma, N., Drain, D., Ganguli, D., Hatfield-Dodds, Z., Hernandez, D., Jones, A., Kernion, J., Lovitt, L., Ndousse, K., Amodei, D., Brown, T., Clark, J., Kaplan, J., McCandlish, S., and Olah, C. A mathematical framework for transformer circuits. *Transformer Circuits Thread*, 2021. <https://transformer-circuits.pub/2021/framework/index.html>.
- Ethayarajh, K. How contextual are contextualized word representations? comparing the geometry of bert, elmo, and gpt-2 embeddings. In *Conference on Empirical Methods in Natural Language Processing*, 2019. URL <https://api.semanticscholar.org/CorpusID:202120592>.
- Farquhar, S., Kossen, J., Kuhn, L., and Gal, Y. Detecting hallucinations in large language models using semantic entropy. *Nature*, 630:625 – 630, 2024. URL <https://api.semanticscholar.org/CorpusID:270615909>.
- Gao, C., Chen, H., Xiao, C., Chen, Z., Liu, Z., and Sun, M. H-neurons: On the existence, impact, and origin of hallucination-associated neurons in llms. 2025. URL <https://api.semanticscholar.org/CorpusID:283450651>.
- Gunasekar, S., Lee, J. D., Soudry, D., and Srebro, N. Characterizing implicit bias in terms of optimization geometry. *ArXiv*, abs/1802.08246, 2018. URL <https://api.semanticscholar.org/CorpusID:3484600>.
- Guss, W. H. and Salakhutdinov, R. On characterizing the capacity of neural networks using algebraic topology. *ArXiv*, abs/1802.04443, 2018. URL <https://api.semanticscholar.org/CorpusID:34916084>.
- Hausmann, J.-C. On the vietoris-rips complexes and a cohomology theory for metric spaces. 1996. URL <https://api.semanticscholar.org/CorpusID:115967265>.
- Hofer, C., Kwitt, R., Niethammer, M., and Uhl, A. Deep learning with topological signatures. *ArXiv*, abs/1707.04041, 2017. URL <https://api.semanticscholar.org/CorpusID:1011245>.
- Ji, Z. and Telgarsky, M. Directional convergence and alignment in deep learning. *ArXiv*, abs/2006.06657, 2020. URL <https://api.semanticscholar.org/CorpusID:219573767>.
- Ji, Z., Lee, N., Frieske, R., Yu, T., Su, D., Xu, Y., Ishii, E., Bang, Y., Chen, D., Dai, W., Madotto, A., and Fung, P. Survey of hallucination in natural language generation. *ACM Computing Surveys*, 55:1 – 38, 2022. URL <https://api.semanticscholar.org/CorpusID:246652372>.

- Kandpal, N., Deng, H., Roberts, A., Wallace, E., and Raffel, C. Large language models struggle to learn long-tail knowledge. In *International Conference on Machine Learning*, 2022. URL <https://api.semanticscholar.org/CorpusID:253522998>.
- Lee, N., Ping, W., Xu, P., Patwary, M., Shoeybi, M., and Catanzaro, B. Factuality enhanced language models for open-ended text generation. *ArXiv*, abs/2206.04624, 2022. URL <https://api.semanticscholar.org/CorpusID:249538460>.
- Lewis, P., Perez, E., Piktus, A., Petroni, F., Karpukhin, V., Goyal, N., Kuttler, H., Lewis, M., tau Yih, W., Rocktäschel, T., Riedel, S., and Kiela, D. Retrieval-augmented generation for knowledge-intensive nlp tasks. *ArXiv*, abs/2005.11401, 2020. URL <https://api.semanticscholar.org/CorpusID:218869575>.
- Li, C., Farkhoor, H., Liu, R., and Yosinski, J. Measuring the intrinsic dimension of objective landscapes. *ArXiv*, abs/1804.08838, 2018. URL <https://api.semanticscholar.org/CorpusID:13739955>.
- Lin, S. C., Hilton, J., and Evans, O. Truthfulqa: Measuring how models mimic human falsehoods. In *Annual Meeting of the Association for Computational Linguistics*, 2021. URL <https://api.semanticscholar.org/CorpusID:237532606>.
- Liu, Y., Tian, X., Sun, Z., and Hu, W. Fine-tuning generative large language models with discrimination instructions for knowledge graph completion. In *International Workshop on the Semantic Web*, 2024. URL <https://api.semanticscholar.org/CorpusID:271334225>.
- Lu, C., Gallagher, J., Michala, J., Fish, K., and Lindsey, J. The assistant axis: Situating and stabilizing the default persona of language models. 2026. URL <https://api.semanticscholar.org/CorpusID:284737822>.
- Maynez, J., Narayan, S., Bohnet, B., and McDonald, R. On faithfulness and factuality in abstractive summarization. *arXiv preprint arXiv:2005.00661*, 2020.
- Merullo, J., Vatsavaya, S., Bushnaq, L., and Lewis, O. From memorization to reasoning in the spectrum of loss curvature. *ArXiv*, abs/2510.24256, 2025. URL <https://api.semanticscholar.org/CorpusID:282401354>.
- Nakkiran, P., Kaplun, G., Bansal, Y., Yang, T., Barak, B., and Sutskever, I. Deep double descent: where bigger models and more data hurt. *Journal of Statistical Mechanics: Theory and Experiment*, 2021, 2019. URL <https://api.semanticscholar.org/CorpusID:207808916>.
- Orgad, H., Toker, M., Gekhman, Z., Reichart, R., Szpektor, I., Kotek, H., and Belinkov, Y. Llms know more than they show: On the intrinsic representation of llm hallucinations. *ArXiv*, abs/2410.02707, 2024. URL <https://api.semanticscholar.org/CorpusID:273098472>.
- Recanatesi, S., Bradde, S., Balasubramanian, V., Steinmetz, N. A., and Shea-Brown, E. A scale-dependent measure of system dimensionality. *Patterns*, 3, 2020. URL <https://api.semanticscholar.org/CorpusID:229549825>.
- Ren, Y. and Sutherland, D. J. Learning dynamics of llm finetuning. *ArXiv*, abs/2407.10490, 2024. URL <https://api.semanticscholar.org/CorpusID:271213641>.
- Rieck, B. A., Togninalli, M., Bock, C., Moor, M., Horn, M., Gumbsch, T., and Borgwardt, K. M. Neural persistence: A complexity measure for deep neural networks using algebraic topology. *ArXiv*, abs/1812.09764, 2018. URL <https://api.semanticscholar.org/CorpusID:53340521>.
- Ruscio, V., Nanni, U., and Silvestri, F. What are you sinking? a geometric approach on attention sink. *ArXiv*, abs/2508.02546, 2025. URL <https://api.semanticscholar.org/CorpusID:280421333>.
- Soudry, D., Hoffer, E., Gunasekar, S., and Srebro, N. The implicit bias of gradient descent on separable data. *ArXiv*, abs/1710.10345, 2017. URL <https://api.semanticscholar.org/CorpusID:3994909>.
- Sriramanan, G., Bharti, S., Sadasivan, V. S., Saha, S., Kattakinda, P., and Feizi, S. Llm-check: Investigating detection of hallucinations in large language models. *Advances in Neural Information Processing Systems* 37, 2024. URL <https://api.semanticscholar.org/CorpusID:276185315>.
- Su, W., Wang, C., Ai, Q., YiRan, H., Wu, Z., Zhou, Y., and Liu, Y. Unsupervised real-time hallucination detection based on the internal states of large language models. In *Annual Meeting of the Association for Computational Linguistics*, 2024. URL <https://api.semanticscholar.org/CorpusID:268351309>.

Suresh, P., Stanley, J., Joseph, S., Scimeca, L., and Bzdok, D. From noise to narrative: Tracing the origins of hallucinations in transformers. *ArXiv*, abs/2509.06938, 2025. URL <https://api.semanticscholar.org/CorpusID:281204242>.

Valeriani, L., Doimo, D., Cuturello, F., Laio, A., Ansuini, A., and Cazzaniga, A. The geometry of hidden representations of large transformer models. *ArXiv*, abs/2302.00294, 2023. URL <https://api.semanticscholar.org/CorpusID:256459698>.

Zhang, Y., Li, Y., Cui, L., Cai, D., Liu, L., Fu, T., Huang, X., Zhao, E., Zhang, Y., Chen, Y., Wang, L., Luu, A. T., Bi, W., Shi, F., and Shi, S. Siren's song in the ai ocean: A survey on hallucination in large language models. *ArXiv*, abs/2309.01219, 2023. URL <https://api.semanticscholar.org/CorpusID:261530162>.

A. Appendix

A.1. Component-Level Mechanisms

Methodology We identify components exhibiting differential behavior. For each MLP neuron, we compute a selectivity score $(\mu_i^{\mathcal{U}} - \mu_i^{\mathcal{F}})/(\sigma_i^{\mathcal{U}} + \sigma_i^{\mathcal{F}})$ using Welford’s online algorithm (Efanov et al., 2021) for memory efficiency. For each attention head, we compute entropy divergence between classes. These component-level analyses highlight candidate architectural loci of detection and identify circuits whose modulation may restore coupling between detection and expression.

Analysis Decomposing residual updates into attention and MLP contributions shows asymmetric involvement in hallucination: at layer 27 in Qwen-2.5, hallucinatory inputs exhibit strong alignment with MLP outputs ($\text{mlp_align} \approx +0.268$) but minimal alignment with attention outputs ($\text{attn_align} \approx +0.017$). This indicates that associative transformations in MLP layers dominate movement along the hallucination direction, while attention provides little corrective signal. Attention sink behavior further differentiates input classes: in fact, in Mistral v0.1 7B at layer 31, factual inputs allocate approximately 88% of attention to the sink position, whereas hallucinatory inputs allocate only $\approx 49\%$, as we can see in Table 1. For hallucinations, attention remains active but diffuse: elevated entropy reflects unsuccessful retrieval of grounding evidence. In the absence of anchoring context, generation becomes dominated by MLP-driven priors. Final-layer statistics show two hallucination regimes: *high-entropy guessing* that arises when representational fracture is severe, yielding flat output distributions; and *confident hallucination* that occurs when fragments align with strong priors, producing low surprisal despite incorrectness. Both regimes exhibit extreme activation kurtosis: correct predictions show values between 7–16, whereas hallucinations reach 280–350. Rather than emerging from distributed consensus, hallucinated outputs are driven by a small number of outlier features.

A.2. Developmental Trajectory

For training dynamics, we apply the full metric suite at each checkpoint, tracking when the LID gap emerges, when low-sensitivity reservoirs form, how Fisher sensitivity evolves, and when gradient blockage develops.

OLMo and Pythia checkpoints show that hallucination-related geometry emerges through distinct training stages. Early in training, factual and hallucinatory inputs are geometrically similar: at OLMo step 1,000, $\text{LID}_{\text{Fact}} \approx 12.6$ versus $\text{LID}_{\text{Hal}} \approx 14.9$. Representations remain largely unstructured, and hallucinations resemble noise. As training progresses, factual representations compress onto low-dimensional manifolds. By step 10,000, factual LID drops to ≈ 10.5 . At the same time, gradient-based coupling between detection and output begins to emerge, and low-sensitivity reservoirs organize into structured subspaces. The model increasingly separates known from unknown. By step 100,000, $\text{LID}_{\text{Fact}} \approx 14.8$ while $\text{LID}_{\text{Hal}} \approx 22.0$ and $\text{LID}_{\text{Imp}} \approx 25.0$. Hallucinations retain partial structure (lower isotropy than impossible inputs), remaining coherent enough to activate readout but too diffuse to support accuracy. Comparing base checkpoints to instruction-tuned models shows that alignment fundamentally alters the detection-expression pathway: Fisher sensitivity collapses and gradient coupling weakens. Although geometric separation between factual and uncertain inputs persists, its functional influence on output is largely suppressed.

A.3. Additional Tables and Plots

A.4. Possible Interventions

Our findings suggest that hallucination arises from a failure to couple internal uncertainty detection to output behavior. This reframing implies that mitigation should focus not on improving detection, but on restoring this integration. We outline several geometry-aware interventions motivated directly by our measurements.

A.4.1. PRETRAINING-TIME INTERVENTIONS.

Checkpoint analysis indicates that hallucination-relevant structure emerges primarily during pretraining. Uncertain inputs are characterized by elevated intrinsic dimensionality and fragmented geometry. This suggests a regularization target: auxiliary losses that penalize LID spikes in the residual stream could encourage uncertain representations to collapse toward a compact uncertainty schema rather than diffuse across disconnected components. Similarly, because high-magnitude activity concentrates in low-sensitivity subspaces weakly coupled to output, one may explicitly anchor a dedicated uncertainty token (e.g., `<uncertain>`) to these directions and train it to activate when internal magnitude is high but vocabulary visibility is low, providing a learnable pathway for abstention.

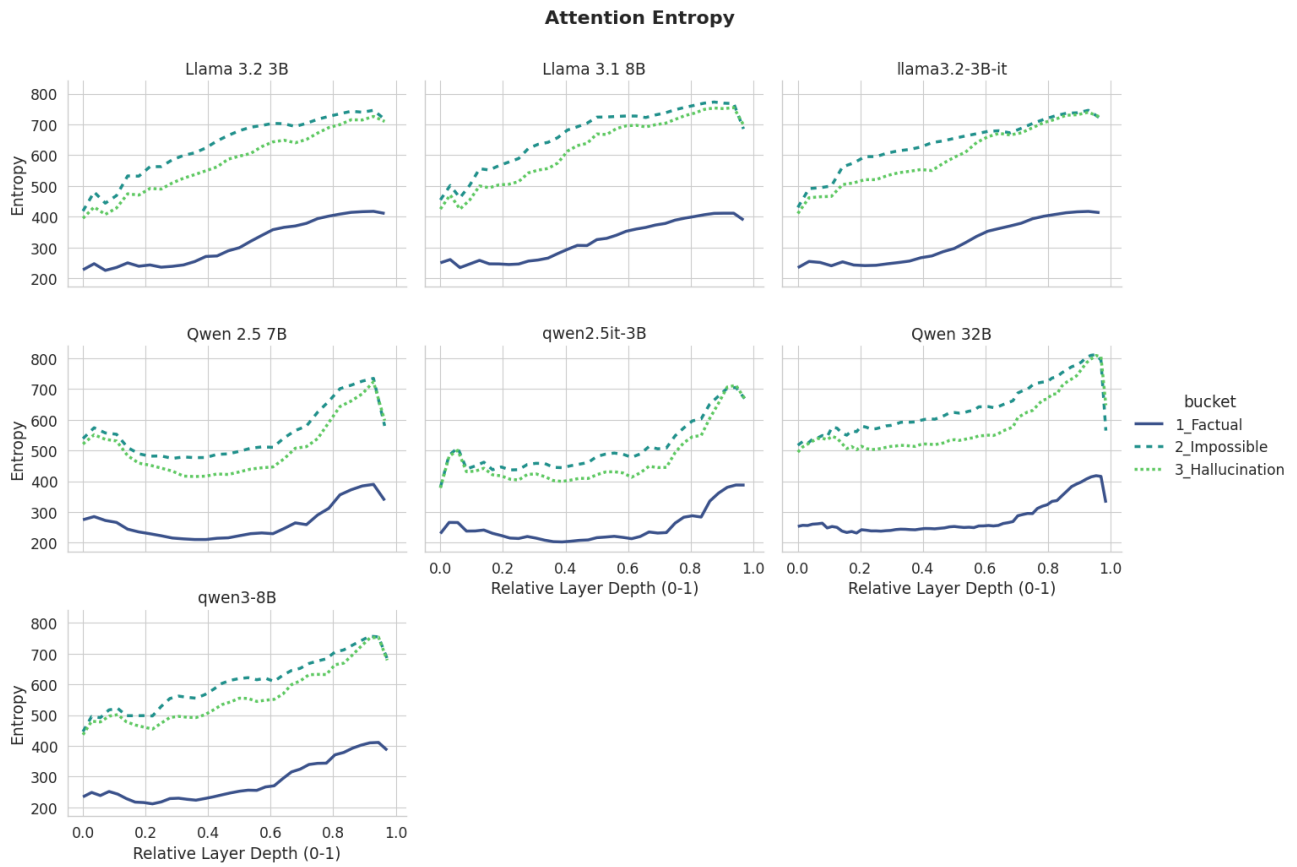


Figure 4. Attention Entropy over different architectures.

A.4.2. ALIGNMENT-TIME INTERVENTIONS.

Comparing base and instruction-tuned models shows that alignment systematically suppresses Fisher sensitivity and gradient coupling along the uncertainty boundary, even though geometric detection remains intact. This motivates geometry-aware preference optimization: rather than penalizing refusals uniformly, alignment objectives could weight updates by Fisher sensitivity or boundary visibility, targeting precisely those regions where detection is present but output sensitivity has collapsed. Component-level analysis further suggests strengthening attention relative to MLPs in late layers, for example, by selectively damping MLP contributions during alignment, so that generation depends more strongly on contextual grounding than associative completion.

A.4.3. INFERENCE-TIME INTERVENTIONS.

When retraining is impractical, several geometric signatures provide actionable decoding-time signals. Hallucinations exhibit extreme final-layer kurtosis, reflecting reliance on sparse outlier features rather than distributed evidence. Monitoring kurtosis jointly with entropy enables dynamic temperature scaling to flatten overconfident logits and promote hedged or abstaining outputs. The boundary direction itself also offers a control handle: projecting residual activations onto this axis and attenuating the uncertain component prior to MLP amplification can prevent uncertainty stored in low-sensitivity subspaces from leaking into vocabulary-aligned directions.

Together, these interventions operationalize our central result: models already encode epistemic uncertainty. The challenge is not detection, but enabling that signal to meaningfully influence generation.

A.5. Extended Related Work

Intrinsic Dimensionality and Representation Geometry. A growing body of work has studied the effective dimensionality of neural representations as a lens into model behavior and generalization. Early investigations by Ansuini et al. (Ansuini et al., 2019) showed that deep networks progressively compress representations into low-dimensional manifolds, with task-relevant information concentrating in a small number of directions. Subsequent studies extended this perspective across architectures and tasks, linking intrinsic dimensionality to expressivity, robustness, and generalization (Valeriani et al., 2023; Li et al., 2018; Recanatani et al., 2020).

In language models, representational geometry has been used to analyze memorization, abstraction, and concept organization (Ethayarajh, 2019; Elhage et al., 2021). Dimensional collapse has also been associated with learning dynamics and feature specialization (Nakkiran et al., 2019). While prior work primarily considers intrinsic dimensionality as a function of task difficulty or training progress, we apply it to characterize epistemic regimes, showing that uncertain inputs consistently occupy higher-dimensional manifolds than factual ones across architectures and modalities.

Topological Analysis of Neural Representations. Topological data analysis (TDA), and persistent homology in particular, has been increasingly applied to study the global structure of neural representations (Guss & Salakhutdinov, 2018; Rieck et al., 2018). These methods have been used to identify class separability, phase transitions during training, and structural complexity of learned manifolds. Recent work has shown that topology can reveal differences between random and trained networks, as well as between robust and brittle representations (Hofer et al., 2017; Chen, 2022).

Decision Geometry and Confidence Dynamics. The geometry induced by softmax classifiers partitions representation space into Voronoi-like regions associated with vocabulary embeddings (Aurenhammer & Klein, 2021). Optimization under cross-entropy encourages representations to move away from decision boundaries and deeper into class basins, increasing margin (Soudry et al., 2017; Ji & Telgarsky, 2020). In deep networks, this dynamic has been linked to feature amplification and confidence calibration, with gradients implicitly driving representations toward simplex vertices.

Training Dynamics and Alignment Effects. Recent work has highlighted how representation structure evolves over training, with early layers forming general-purpose features and deeper layers specializing toward task objectives (Nakkiran et al., 2019). Studies of fine-tuning and alignment have further shown that post-training can substantially reshape internal representations and confidence calibration, often trading robustness for helpfulness or fluency.

A.6. Datasets

Here we present a sample of the datasets we generated using Claude and Gemini, and that we also manually checked. In the supplementary materials you can find the full datasets.

The evaluation datasets were constructed to isolate distinct epistemic regimes rather than to maximize difficulty per se. The Factual Knowledge dataset, as we can see in Table 8 was intentionally composed of simple, high-confidence questions (e.g., capitals, authorship, basic scientific facts) on which contemporary models achieve consistently high accuracy. This ensures that representations in this regime reflect genuine model knowledge, providing a stable geometric baseline for comparison.

In contrast, the Impossible Questions dataset, as we can see in Table 9 was explicitly designed to elicit confabulation by presenting prompts that cannot be answered meaningfully. These include both false-presupposition questions (e.g., anachronistic or logically inconsistent premises) and context-deficient queries that lack sufficient information for resolution. Multiple prompt styles were used to avoid stylistic bias and to probe whether models recognize unanswerability across diverse linguistic forms.

For diffusion models, the Paradoxical Prompts dataset targets well-documented failure modes by requesting internally inconsistent or combinatorially constrained scenes, such as precise object counts, specific color assignments, legible text, or coherent spatial layouts. These prompts describe plausible scenarios but impose requirements that current text-to-image systems systematically fail to satisfy, allowing us to probe uncertainty-related geometry in continuous generative settings.

Together, these datasets enable controlled comparisons between grounded knowledge, meaningful but unanswerable inputs, and hallucination-prone regimes, ensuring that observed geometric effects reflect epistemic structure rather than generic task difficulty.

A.7. Hallucinations in generated pictures

To characterize the temporal dynamics of hallucination in continuous output spaces, we probe the generation trajectory of the PixArt- Σ (XL-2-1024-MS) Diffusion Transformer. We implement an intermediate latent decoding protocol. During the standard 20-step denoising schedule (DDIM), we intercept the latent state z_t at steps $t = 0, 5, 10, 15, 19$. At each intercept, we decode the noisy latents through the VAE to visualize the model’s current internal representation of the prompt. This allows us to observe the specific moment where the model commits to a visual concept and to visualize how the “fractured geometry” observed in our quantitative analysis manifests as visual incoherence or semantic drift.

For paradoxical prompts, we observe two distinct failure modes that align with our geometric findings:

- The model ignores the conflict and hallucinates a standard object. For the prompt in Figure 5c (“A daguerreotype of Ancient Greek philosophers”) it might generate standard people at Step 5, and add the hallucinated faces by Step 15. The impossible constraint is overridden by the strongest prior, mirroring the “confident hallucination” seen in robust LLMs.
- The model fails to resolve the global composition. At Step 5 and 10, the image remains amorphous or structurally inconsistent, as we can see in Figure 5e. The visual output remains “blurry” or geometrically impossible until the final step, reflecting the high Local Intrinsic Dimensionality (LID) of the latent state. The model cannot collapse the wavefunction of the image because the prompt maps to a fractured manifold with no single energy minimum.

These visualisations visually show that “visual hallucination” is not merely an error of the final output, but a dynamical process. Paradoxical inputs prevent the diffusion process from settling into a low-dimensional manifold, forcing the model to either drift away from the prompt (decoupling) or produce high-entropy, incoherent artifacts (fracture).

A.8. Metrics Overview

Our analysis combines geometric, functional, and component-level metrics designed to characterize how uncertainty is represented and propagated through the network. Below we summarize the principal quantities used throughout the paper. Throughout, “uncertain” refers to the union of Impossible and Hallucination inputs unless stated otherwise.

Boundary Vector For each layer l , we define the boundary vector

$$b_l = \frac{\mu_l^{\mathcal{U}} - \mu_l^{\mathcal{F}}}{\|\mu_l^{\mathcal{U}} - \mu_l^{\mathcal{F}}\|} \quad (2)$$

as the normalized difference between class centroids of uncertain (\mathcal{U}) and factual (\mathcal{F}) inputs. This direction operationalizes the model’s internal axis of answerability. We track the boundary norm $\|\mu_l^{\mathcal{U}} - \mu_l^{\mathcal{F}}\|$ to measure class separation and the boundary stability $\cos(b_l, b_{l-1})$ to assess directional consistency across layers.

Local Intrinsic Dimensionality (LID) LID estimates the effective dimensionality of representations in a local neighborhood:

$$\text{LID}(x) = - \left(\frac{1}{k} \sum_{i=1}^k \log \frac{r_i}{r_k} \right)^{-1} \quad (3)$$

where r_i are distances to the k nearest neighbors. High LID indicates diffuse, high-dimensional geometry; low LID reflects compression onto structured manifolds.

Spectral Geometry We compute the eigenspectrum of within-class hidden-state covariance matrices. Isotropy is defined as λ_2/λ_1 , the ratio of the second to first principal component variances. Spectral entropy

$$H = - \sum_i \hat{\sigma}_i \log \hat{\sigma}_i \quad (4)$$

(with normalized singular values $\hat{\sigma}_i$) provides a continuous measure of effective dimensionality. We additionally report the number of principal components explaining 90% of variance.

Topological Complexity To characterize representational fragmentation, we apply persistent homology to points near the geometric boundary. Zeroth Betti number β_0 counts connected components, while β_1 counts loops. Increasing β_0 indicates topological fracture of the uncertainty manifold.

Fisher Sensitivity We estimate sensitivity of the output distribution to perturbations along the boundary:

$$F(b_l) \approx \epsilon^{-2} D_{\text{KL}}^{\text{sym}} [p(y|h_l) \| p(y|h_l + \epsilon b_l)] \quad (5)$$

Low Fisher sensitivity values indicate that movement along the uncertainty direction has little effect on output probabilities.

Hessian Curvature Curvature along the boundary is approximated via finite differences:

$$H(b_l) \approx \epsilon^{-2} [\mathcal{L}(h_l + \epsilon b_l) - 2\mathcal{L}(h_l) + \mathcal{L}(h_l - \epsilon b_l)] \quad (6)$$

where \mathcal{L} is negative log-likelihood. Near-zero curvature indicates a flat loss landscape along the uncertainty axis.

Jacobian Amplification We estimate directional Jacobian amplification along the boundary as:

$$\text{amp}_l = \epsilon^{-1} \|\text{Layer}_l(h + \epsilon b_l) - \text{Layer}_l(h)\|. \quad (7)$$

Values above one indicate amplification of uncertainty-related perturbations.

Gradient Blockage To assess coupling between detection and expression, we compute

$$\text{blockage}_l = \cos(\nabla_{h_l} \sum_{k \in \mathcal{U}} z_k, b_l) \quad (8)$$

where \mathcal{U} denotes uncertainty-related tokens. Near-zero values indicate geometric decoupling between uncertainty representations and output gradients.

Low-Sensitivity Ratio Using the SVD of the unembedding matrix $W_U = U\Sigma V^\top$, we define visible subspaces $\mathcal{V}_m = \text{span}\{v_1, \dots, v_m\}$. The low-sensitivity ratio of a vector x is

$$\text{lowSens}_m(x) = \frac{\|P_{\mathcal{V}_m^\perp} x\|}{\|x\|} \quad (9)$$

quantifying how much representational energy lies in directions weakly coupled to vocabulary logits.

Component Metrics We measure alignment of attention and MLP outputs with the boundary vector, attention entropy and sink mass, final-layer kurtosis, and token surprisal. Together these characterize how uncertainty propagates through architectural components and how hallucinated outputs are constructed.

All metrics are computed on post-residual hidden states at the final token position (or spatially averaged latents for diffusion models).

Table 5. **Cross-Model Geometric Comparison.** Aggregated metrics showing the separation between factual and hallucinatory geometry across 8 architectures. Boundary Norm scales vary by model architecture.

Model	Type	Eval Set	Norm	Stability	Fisher	Hessian	Jac. Amp
llama3.1-8B	Hallucination	Factual	5.684	0.761	0.050	0.012	1.275
	Hallucination	Hallucination	5.684	0.761	0.055	0.026	1.204
	Impossible	Factual	7.521	0.767	0.057	0.015	1.292
	Impossible	Impossible	7.521	0.767	0.076	0.020	1.237
llama3.2-3B	Hallucination	Factual	4.940	0.749	0.043	0.018	1.269
	Hallucination	Hallucination	4.940	0.749	0.049	0.023	1.179
	Impossible	Factual	6.437	0.751	0.043	0.017	1.285
	Impossible	Impossible	6.437	0.751	0.073	0.021	1.211
llama3.2-3B-it	Hallucination	Factual	5.077	0.763	0.213	0.014	1.282
	Hallucination	Hallucination	5.077	0.763	0.459	0.019	1.236
	Impossible	Factual	6.592	0.760	0.229	0.017	1.298
	Impossible	Impossible	6.592	0.760	0.547	0.011	1.279
mistralv1-7B	Hallucination	Factual	21.640	0.948	0.089	0.039	1.097
	Hallucination	Hallucination	21.640	0.948	0.326	-0.013	1.097
	Impossible	Factual	23.019	0.948	0.375	0.040	1.123
	Impossible	Impossible	23.019	0.948	1.239	-0.010	1.122
qwen2.5-7B	Hallucination	Factual	26.896	0.724	0.333	-0.005	1.741
	Hallucination	Hallucination	26.896	0.724	0.404	0.001	1.560
	Impossible	Factual	33.585	0.718	0.323	-0.004	1.769
	Impossible	Impossible	33.585	0.718	0.325	0.000	1.606
qwen2.5it-3B	Hallucination	Factual	15.580	0.738	1.913	0.003	1.674
	Hallucination	Hallucination	15.580	0.738	4.649	-0.003	1.567
	Impossible	Factual	19.716	0.730	1.803	0.005	1.642
	Impossible	Impossible	19.716	0.730	4.421	-0.004	1.566
qwen3-32B	Hallucination	Factual	71.879	0.866	0.353	0.000	2.212
	Hallucination	Hallucination	71.879	0.866	0.793	-0.001	2.037
	Impossible	Factual	97.859	0.869	0.378	0.000	2.220
	Impossible	Impossible	97.859	0.869	1.451	-0.002	2.071
qwen3-8B	Hallucination	Factual	54.354	0.795	1.273	0.000	2.107
	Hallucination	Hallucination	54.354	0.795	1.203	0.004	2.044
	Impossible	Factual	69.349	0.785	1.383	-0.000	2.135
	Impossible	Impossible	69.349	0.785	0.762	0.003	1.996

Table 6. Intrinsic dimension (LID), Isotropy, and Entropy aggregated by bucket.

Model	Bucket	LID	Isotropy	Entropy
llama3.1-8B	Factual	11.79	0.6590	319.9
	Impossible	18.05	0.5190	664.0
	Hallucination	15.09	0.6970	618.8
llama3.2-3B	Factual	11.70	0.5810	312.9
	Impossible	17.83	0.5450	633.0
	Hallucination	14.53	0.7040	578.6
llama3.2-3B-it	Factual	11.97	0.6090	314.7
	Impossible	17.59	0.6180	635.4
	Hallucination	14.56	0.6050	596.8
qwen2.5-7B	Factual	9.71	0.5820	265.7
	Impossible	14.27	0.4060	554.4
	Hallucination	12.62	0.5110	507.1
qwen2.5it-3B	Factual	9.83	0.5810	250.4
	Impossible	14.16	0.4620	507.9
	Hallucination	12.48	0.5480	470.9
qwen3-32B	Factual	10.41	0.5410	279.2
	Impossible	16.76	0.5240	636.5
	Hallucination	14.70	0.5430	579.5
qwen3-8B	Factual	11.21	0.5480	282.7
	Impossible	15.63	0.6170	603.1
	Hallucination	13.96	0.5620	560.1

Table 7. Aggregated Attention and Logit metrics by model and condition.

Model	Bucket	Attn. Ent.	Attn. Sink	Res. Norm	Confidence
llama3.1-8B	Factual	0.96	0.716	18.5	0.047
	Hallucinations	1.06	0.701	18.8	0.024
	Impossible	1.01	0.703	19.0	0.022
llama3.2-3B	Factual	0.87	0.736	16.7	0.048
	Hallucinations	1.01	0.709	17.5	0.020
	Impossible	0.96	0.713	17.6	0.025
llama3.2-3Bit	Factual	0.85	0.756	16.1	0.057
	Hallucinations	0.97	0.733	16.6	0.030
	Impossible	0.96	0.723	16.7	0.032
mistralv1-7B	Factual	1.16	0.227	50.6	0.094
	Hallucinations	1.12	0.154	43.8	0.064
	Impossible	1.01	0.153	46.5	0.071
qwen2.5-7B	Factual	1.17	0.535	108.0	0.251
	Hallucinations	1.27	0.521	106.9	0.244
	Impossible	1.17	0.540	109.1	0.268
qwen2.5it-3B	Factual	1.20	0.452	85.5	0.187
	Hallucinations	1.28	0.445	86.1	0.189
	Impossible	1.21	0.458	85.4	0.212
qwen3-32B	Factual	0.66	0.005	329.2	0.269
	Hallucinations	0.72	0.005	324.4	0.266
	Impossible	0.69	0.006	341.3	0.270
qwen3-8B	Factual	1.05	0.557	222.8	0.330
	Hallucinations	1.13	0.546	224.3	0.312
	Impossible	1.09	0.549	230.3	0.324

The Phenomenology of Hallucinations

Question	Answer	Category
What is the capital of Greece?	Athens	Capitals
What is the capital of Poland?	Warsaw	Capitals
What is the capital of Sweden?	Stockholm	Capitals
Who wrote <i>Wuthering Heights</i> ?	Emily Brontë	Authors
Who wrote <i>Frankenstein</i> ?	Mary Shelley	Authors
Who wrote <i>Dracula</i> ?	Bram Stoker	Authors
Who founded Twitter?	Jack Dorsey	Companies
Who founded Nike?	Phil Knight	Companies
Who founded Walmart?	Sam Walton	Companies
What is the unit of force?	Newton	Science
What is the unit of energy?	Joule	Science

Table 8. Representative examples from the Factual Knowledge dataset. Each entry consists of a question, its verified answer, and semantic category.

Impossible questions Dataset Samples

Wrong premise questions

What is the ISBN of Albert Einstein’s 1957 cookbook ‘Relativity Recipes’?
 What social media platform did Julius Caesar use to announce his victories?
 What was George Washington’s TikTok username?
 What is the patent number for Leonardo da Vinci’s microwave oven?
 How tall was Napoleon’s pet dinosaur?
 What is the entrance fee for the Forbidden City in Rio de Janeiro?
 How fast can a goblin run in kilometers per hour?
 What was Genghis Khan’s email address?

No context questions

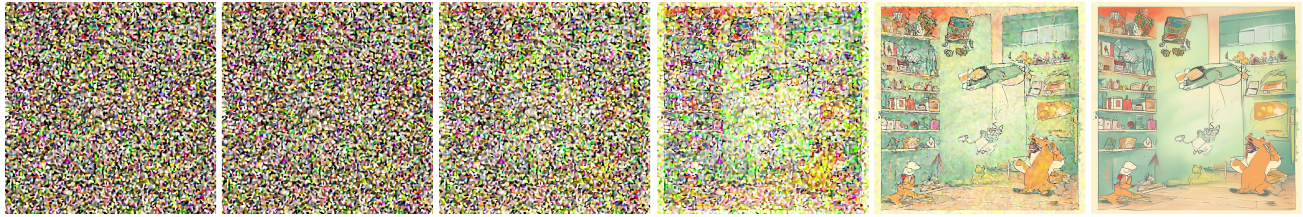
Who won the Super Bowl that year?
 How much does it cost?
 Did the database sync?
 Is the API public?
 Does it support wireless charging?
 Did the patch fix the bug?
 How many megapixels is the camera?
 Is the server online?
 Is the warranty transferable?
 What is the discount code?

Table 9. Representative examples from the Impossible questions dataset.

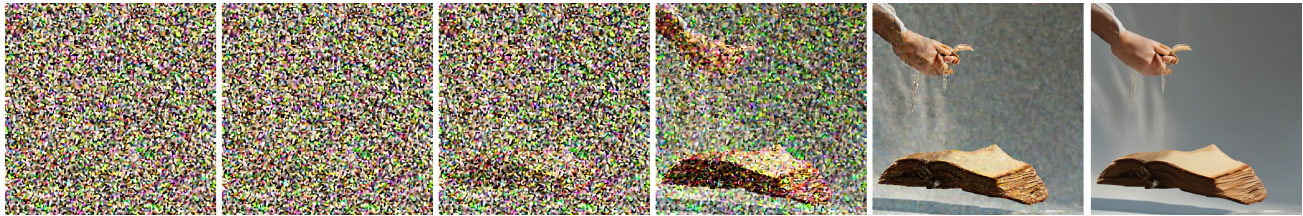
Paradox Prompts Dataset Samples

A digital clock display showing exactly 09:07 (leading zero required).
 ”A photo of exactly 7 apples in a straight line, all visible and not overlapping.”
 A desk with exactly 9 paperclips arranged in a 3×3 grid.
 A beach scene with exactly 5 umbrellas, each a different color, all fully visible.
 A red cube, a blue sphere, and a green pyramid, left to right in that order.
 ”A dog wearing sunglasses and a cat wearing a bowtie, plus another dog wearing a bowtie and another cat wearing sunglasses (four animals total).”
 A person holding a sign above their head; the sign is readable and not tilted.
 A floating book that is visibly not supported by strings, hands, or surfaces (clean background).

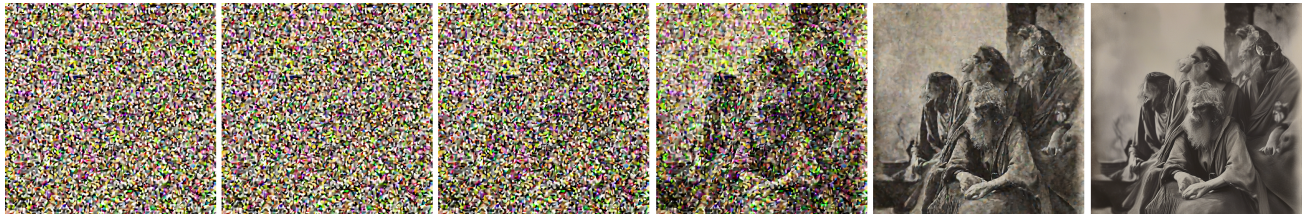
Table 10. Representative examples from the Paradox prompts dataset for image generation.



(a) Intermediate steps to generate an output from the prompt: "A classroom poster that reads exactly: THE QUICK BROWN FOX JUMPS OVER THE LAZY DOG."



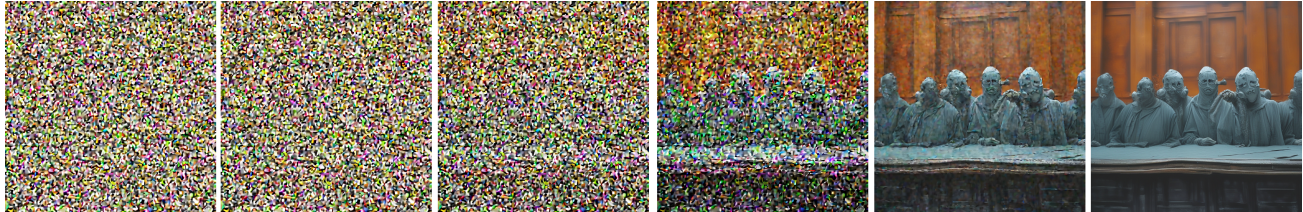
(b) Intermediate steps to generate an output from the prompt: "A floating book that is visibly not supported by strings, hands, or surfaces (clean background)."



(c) Intermediate steps to generate an output from the prompt: "A daguerreotype of Ancient Greek philosophers"



(d) Intermediate steps to generate an output from the prompt: "A courtroom scene where everyone is wearing scuba gear."



(e) Intermediate steps to generate an output from the prompt: "A cup to the left of a plate, and a bowl to the right of the plate (three objects aligned)."

Figure 5. Examples of intermediate steps in generating images from a prompt that leads to hallucinations.